ACS APPLIED ENERGY MATERIALS

www.acsaem.org Article

Systematic Design and Synthesis of Conjugated Microporous Polymers Containing Pyrene and Azobenzene Building Materials for High-Performance Energy Storage

Poonam Nagendra Singh,[#] Mohamed Gamal Mohamed,[*,#] and Shiao-Wei Kuo[*]

Cite This: *ACS Appl. Energy Mater.* 2023, 6, 11342−11351 Read Online

ACCESS | Metrics & More | Article Recommendations | Supporting Information

ABSTRACT: Conjugated microporous polymers (CMPs), known for their high specific capacities, exceptional cycling stability, and outstanding rate performance, are being actively studied as advanced electrode materials for energy storage applications. The utilization of redox-active units in CMP materials in energy storage exhibits substantial promise. Nevertheless, the influence of the positioning of the redox-active region on the electrochemical behavior and battery performance remains a topic of uncertainty. Herein, we successfully created two CMPs using the Sonogashira−Hagihara coupling method, specifically by including redox-active azobenzene (Azo) moieties in the *meta* (*m*) and *para* (*p*) locations. These CMPs are named Py-*m*Azo-CMP and Py-*p*Azo-CMP. To produce them, we used precursor compounds (*E*)-1,2-bis(3-bromophenyl)diazene (*m*Azo-Br_2) and (*E*)-1,2-bis(4-bromophenyl)diazene (*p*Azo-Br_2), combined with tetraethynylpyrene (Py-T). Our primary focus was to investigate the impact of substituting the Azo unit at different positions. To assess the orientation of molecules and the pores of these Py-Azo-CMPs, we conducted a thorough analysis, including BET isotherm measurements and various spectroscopic and microscopic techniques. Our findings from TGA analysis indicated that these Py-Azo-CMPs exhibit a moderate thermal stability. One remarkable discovery was the excellent electrochemical performance of Py-*p*Azo-CMP, which displayed a capacitance of 142 F g^{-1} (determined at 1 A g^{-1}), showcasing its exceptional capacitive properties. Despite operating at a substantial current density of 10 A g^{-1}, both Py-*m*Azo and Py-*p*Azo-CMPs exhibited remarkable long-term stability, retaining over 92% of their capacity even after 5000 cycles. These results underscore the potential of Py-*p*Azo-CMP as a dependable and enduring choice for energy storage applications. Our findings highlight the significant promise of these Py-Azo-CMP materials and underscore their suitability for useful applications, including electrical energy storage (EES).

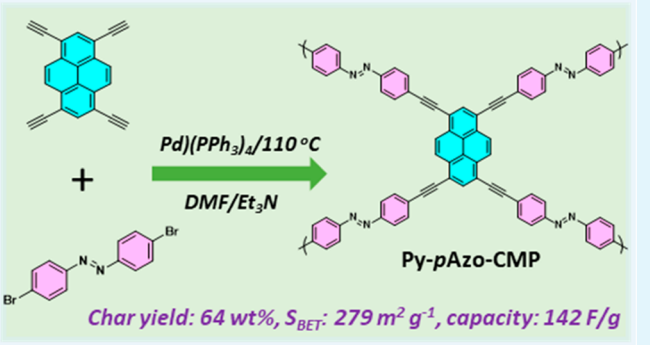

KEYWORDS: *Pyrene, Azobenzene, Sonogashira−Hagihara coupling, Conjugated microporous polymers, Supercapacitor, Symmetric coin supercapacitor*

INTRODUCTION

Energy exerts a profound impact on our quality of life and underpins our societal and economic advancements.[1,2] In a world heavily reliant on energy, electrochemical technologies for energy storage emerge as indispensable tools to combat the depletion of fossil fuels.[3−5] While various options are available to meet these needs, such as harnessing sustainable energy sources including wind, solar, and geothermal power, these sources are not without limitations.[6−10] They not only focus on electricity generation but also grapple with resource scarcity.[5,11,12] Amid these considerations, supercapacitors (SCs) have garnered considerable importance as promising devices that hold energy due to their exceptional attributes. Notably, they boast a high density of power, swift charge and discharge capabilities, as well as extended durability throughout their operational cycles.[13,14]

SCs have been devised to address the pressing challenge of escalating energy consumption, a critical issue in our present times. The driving force behind research in developing such devices is the imminent exhaustion of fossil fuel reserves. Supercapacitors, with their ecofriendly attributes, high specific capacitance, rapid charge−discharge characteristics, and promising energy storage capabilities, find extensive applications across various industries, notably in military applications and the automotive sector, including electric vehicles. Super-

Received: September 5, 2023
Revised: October 12, 2023
Accepted: October 13, 2023
Published: November 1, 2023

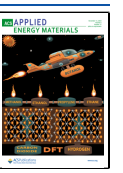

capacitors have made significant strides in research and technology, especially due to their improved energy density, making them a more practical alternative to conventional batteries.[15−21]

Supercapacitors (SCs) primarily store electrical charges through two distinct mechanisms, which depend on the underlying energy storage processes: non-Faradaic processes based on electrochemical double-layer capacitance (EDLC) and Faradaic pseudocapacitance mechanisms resulting from reversible redox reactions occurring within the electrode materials.[5] Electrochemical double-layer capacitors (EDLC) function by accumulating electrostatic charges at the interface of the electrodes and the electrolyte, whereas pseudocapacitors store energy by promoting rapid reactions at the electrode surface, where Faradaic processes take place. The latter, thanks to redox reactions, allows for the attainment of higher specific capacitance values.[22] Porous organic polymers (POPs) are particularly intriguing to researchers in their continuous pursuit of innovative materials due to their exceptional characteristics, which include high porosity, adjustable pore sizes, and substantial effective surface area in both two- and three-dimensional forms.[23−28]

Porous organic polymers (POPs) exhibit diverse forms, with one notable category being conjugated microporous polymers (CMPs).[23−28] These materials offer several benefits compared with substitute microporous organic polymers, particularly when compared to metal−organic frameworks (MOFs) and organic frameworks with covalent bonds (COFs). Such advantages encompass exceptional physical and chemical stability, straightforward synthesis processes, vast surface areas, and heightened microporosity.[23−28] CMPs, a subset of POPs, are amorphous materials that can form 2D or 3D frameworks, enabling the linkage of building blocks in a π-conjugated manner.[29] They have gained significant attention since their discovery by the Cooper group primarily due to their intriguing characteristics, including microporous structures and versatile π-conjugation networks within the framework.

These properties make CMPs highly promising for a broad array in terms of applications, ranging from gas storage to catalytic activities, renewable energy technologies, and metal ion sensing.[30−34] Additionally, the inclusion of heteroatoms like adding nitrogen to the frameworks of microporous conjugated polymers (CMPs) has been demonstrated as a valuable strategy to improve the electrochemical behavior of materials based on CMP.[35,36] As building blocks, CMPs can utilize a wide array of components, including basic aromatic rings, multicyclic aromatics, derivatives of styryl, and heterocyclic molecules. Active groups such as acetylene, cyano, amino, aldehyde, iodine, boric acid, and bromine, among others, can also be incorporated. Consequently, the extensive range with respect to active groups and block units significantly augments the style versatility of CMPs, encompassing both their structural and pore attributes. This makes CMPs a crucial platform for advancing innovative organic porous polymers.[37,38]

CMPs, alongside covalent organic frameworks (COFs), have gained popularity in electrochemical applications for energy storage due to several reasons: (i) their capacity to easily incorporate different compounds and electrode active spot applications; (ii) their capacity to make charge transmission easier, including penetration of electrolytes to control strain and tension experienced during electrochemical reactions; (iii) their capability to facilitate charge transfer through π-conjugated frameworks; and (iv) their potential to construct 2D and 3D structures, extensive regions of surface, thus enhancing the kinetics of electrochemistry. Moreover, the simplicity of CMP construction and their adaptability, featuring a range of redox-active moieties, make them highly suitable for improving the performance of supercapacitors as well as lithium-ion battery (LIB) enhanced reversibility and cyclability.[39]

Azo compounds are organic species characterized by the presence of azo (N═N) groups, and they are recognized as intelligent materials due to their reversible redox activity[40,41] and photosensitivity.[42] These compounds are prized for their ability to undergo a two-electron redox process involving the N═N/NN moiety and their conjugation with aromatic groups, making them valuable as high-capacity active materials and rapid redox responses.[40,41] It has been established that the functionality and molecular architectures of electroactive polymers can be tailored through the use of diverse monomers and linkers.[43] Furthermore, the connection points between these elements can be strategically chosen to modify their electrochemical and photophysical properties. One prevalent approach in energy storage involves the incorporation of reactive oxygen species within the backbone of conjugated polymers. Conjugated materials have been intended to modulate extended systems for electronic communication and have benefited from the influential design principle of *meta*- vs *para*-conjugation.[44,45] Generally, *para* connectivity is favored over *meta* connectivity because it results in a minimized band gap and enhanced conductivity of electricity. This preference arises from its electrical resonance that is effective and a more planar layout, which fosters improved intermolecular interactions.[46,47] The *para*-conjugation design, with its robust electronic communication and consequent low bandgap, finds widespread use in applications such as light-emitting devices and organic solar cells.[44,48]

To be more specific, in conjugated polymers, particularly those with *para*-conjugation, the redox units interact conjugatively and the polarons generated during initial electron injection elevate the lowest empty molecular orbital energy. This makes subsequent infusions of electrons, such as bipolarons, challenging and causes their ability to reduce to shift toward even more negative values. Coulombic charge repulsion primarily accounts for this phenomenon. However, recent findings suggest that polymers that have been conjugated featuring "the side-chain redox units" can mitigate charge repulsion and maintain firm electrical conductive properties via the polymer's main chain.[49] The pyrene component (Py) possesses a flat structure with an extensive π-conjugation.[50,51] Py is utilized to enhance charge transport capabilities in organic semiconductors, where molecular alignment is controlled through π-conjugated systems.[52−56]

In this investigation, we formulated Azo-CMPs based on the use of pyrene as the central building block. We strategically positioned the Azo moiety at both the *m* and *p* positions to investigate its impact on supercapacitance performance. Specifically, we synthesized both CMPs, Py-*m*Azo-CMP, and Py-*p*Azo-CMP, through Sonogashira−Hagihara cross-coupling reactions of *m*Azo-Br_2 and *p*Azo-Br_2 with Py-T, as well, with a Pd catalyst present. Our comprehensive characterization included examination in terms of their chemical compositions, pore size diameters, morphological features, and thermal stabilities. Subsequently, we evaluated the electrochemical

https://doi.org/10.1021/acsaem.3c02252
ACS Appl. Energy Mater. 2023, 6, 11342−11351

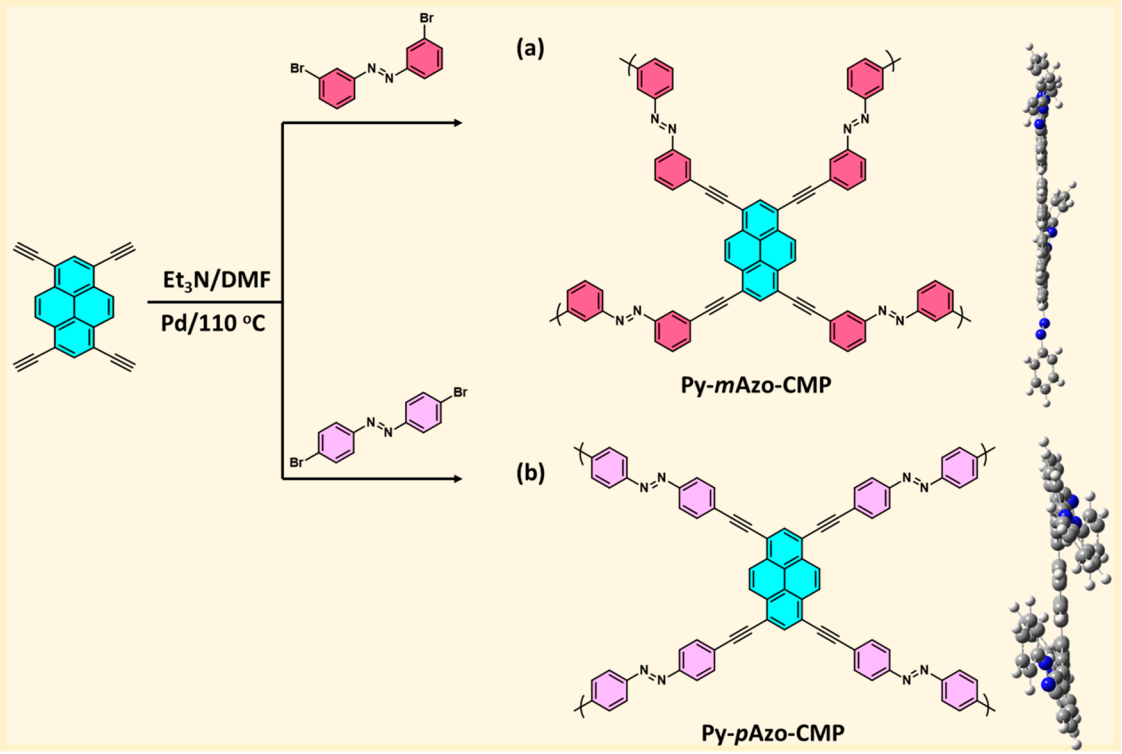

Figure 1. Preparation of (a) Py-*m*Azo and (b) Py-*p*Azo-CMPs.

productivity of these Py-Azo-CMPs in both a three-electrode system and a coin-cell supercapacitor setup.

EXPERIMENTAL SECTION

Materials. Palladium tetrakis(triphenylphosphine) [$Pd(PPh_3)_4$], 4-bromoaniline (97%), 3-bromoaniline (98%), pyridine (99.8%), CuBr (98%), potassium carbonate (K_2CO_3, 99.9%), methanol (MeOH), bromine (Br_2), chloroform ($CHCl_3$), acetone (CH_3COCH_3), triphenylphosphine (PPh_3, 99%), pyrene (Py, 98%), tetrahydrofuran (THF), anhydrous magnesium sulfate ($MgSO_4$, 99.5%), copper(I) iodide (CuI, 99%), and other solvents were purchased commercially from Sigma-Aldrich. 1,3,6,8-Tetrakis(2-(trimethylsilyl)ethynyl) pyrene (Py-TMS) was prepared following established protocols.[57−61]

Synthesis of (*E*)-1,2-Bis(3-bromophenyl)diazene (*m*Azo-Br_2). A 250 mL round-bottom flask was utilized to combine pyridine (144 mL), CuBr (0.075 g), and 3-bromoaniline (3 g) with toluene (75 mL). Using a magnetic stirrer, this mixture was stirred continuously for a duration of 24 h at 60 °C. After the outcome, the solution was permitted to reach room temperature before the solvent was removed, and subsequently, flash chromatography was carried out on the resulting residue utilizing a short silica gel column using hexane. Subsequently, the product was dried and washed with hexane, resulting in the isolation of the desired product, which exhibited an orange solid (Scheme S1). T_m: 128 °C (Figure S1). FTIR (cm^{-1}, Figure S2): 3073, 1571. ^1H NMR (ppm, Figure S3): 8.02, 7.95, 7.78, 7.59. ^{13}C NMR (ppm, Figure S4): 153.44, 135.06, 132.33, 124.07, 123.26. HRMS (ESI, Figure S5): m/z $[M + H]^+$ calcd for $C_{12}H_8N_2Br_2$, 340.0063; found, 340.9108. T_{d10}: 226.52 °C (Figure S6).

Synthesis of (*E*)-1,2-Bis(4-bromophenyl)diazene (*p*Azo-Br_2). A mixture of pyridine (144 mL), CuBr (0.075 g), and 4-bromoaniline (3 g) was combined with toluene (75 mL) in a 250 mL round-bottom flask while being stirred with a magnetic stirrer. This gave the mixture a stir at 60 °C for a duration of 24 h. The solution was then given time to react before being cooled to room temperature. The solvent was subsequently evaporated, and the resulting residue was subjected to flash chromatography on a silica gel column. Afterward, the product was dried and washed with hexane, resulting in the isolation of the desired product, which exhibited an orange solid (Scheme S2). T_m: 210 °C (Figure S7). FTIR (cm^{-1}, Figure S8): 3095, 1567. ^1H NMR (ppm, Figure S9): 7.70, 7.65. ^{13}C NMR (ppm, Figure S10): 152, 133.42, 125.44, 123. HRMS (ESI, Figure S11): m/z $[M + H]^+$ calcd for $C_{12}H_8N_2Br_2$, 340.0063; found, 340.9108. T_{d10}: 246.9 °C (Figure S12).

Synthesis of 1,3,6,8-Tetraethynylpyrene (Py-T). Py-TMS (3.18 g, 5.20 mmol) and K_2CO_3 (5.62 g, 40.8 mmol) were dissolved together with MeOH (40 mL) and stirred for 1 day at 25 °C in a 50 mL round-bottom flask that had a neck. To remove K_2CO_3, 50 mL of water was added to the reaction solution. After filtration and being dried at 60 °C, the outcome of the brown precipitate was observed (2.4 g, Scheme S3).

Synthesis of Py-*m*Azo-CMP and Py-*p*Azo-CMP. A dark-brown solid of Py-*m*Azo-CMP (Figure 1a) was obtained by heating a mixture containing 20 mL of DMF and Et_3N, Py-T (250 mg, 0.84 mmol), *m*Azo-Br_2 (570 mg, 1.68 mmol), CuI (18 mg), PPh_3 (26 mg), and $Pd(PPh_3)_4$ (116 mg) at 110 °C for 72 h. Afterward, the obtained solid, which was insoluble, was separated by filtration and subjected to a series of washes with MeOH and acetone. The solid was then dried at 100 °C for 24 h to yield the final product. Py-*p*Azo-CMP was synthesized using the same procedure as Py-*m*Azo-CMP, with the only difference being the replacement of *m*Azo-Br_2 with *p*Azo-Br_2. This led to the development of a dark brown solid (Figure 1b). The insolubility of Py-*m*Azo-CMP and Py-*p*Azo-CMP in organic solvents like THF, EtOH, DMF, and MeOH is evident, as demonstrated in Figure S13.

RESULTS AND DISCUSSION

Synthesis and Characterization of *m*Azo-Br_2, *p*Azo-Br_2, Py-*m*Azo-CMP, and Py-*p*Azo-CMP. In this study, orange solid monomers, namely, *m*Azo-Br_2 and *p*Azo-Br_2, were synthesized by reacting 3-bromoaniline and 4-bromoaniline with pyridine and toluene, using CuBr as a catalyst (Schemes S1 and S2). The FTIR analysis indicated that there are aromatic C—H and C═C functional groups in both *m*Azo-Br_2

https://doi.org/10.1021/acsaem.3c02252
ACS Appl. Energy Mater. 2023, 6, 11342−11351

and *p*Azo-Br_2, with characteristic peaks that can be detected within the spectral ranges of 3059−3073 cm^{-1} and 1567−1571 cm^{-1} (Figures S1 and S3). The proton aromatic signals were observed at 8.02, 7.95, 7.78, and 7.59 ppm for *m*Azo-Br_2, while, for *p*Azo-Br_2, they were detected at 7.83, 7.52, and 6.85 ppm. Furthermore, the carbon aromatic resonances were identified at 153.44, 135.06, 132.33, 124.07, and 123.26 ppm in the case of *m*Azo-Br_2, whereas, for *p*Azo-Br_2, they were found at 152, 133.42, 125.44, and 123 ppm. We employed Sonogashira−Hagihara couplings to synthesize Py-*m*Azo (Figure 1a) and Py-*p*Azo-CMPs (Figure 1b) by reacting Py-T with *m*Azo-Br_2 and *p*Azo-Br_2, respectively, at a temperature of 110 °C for a duration of 3 days. This process yielded brown powders for both Py-Azo-CMPs. The resultant Py-Azo-CMPs were then thoroughly washed with organic solvents (DMF, MeOH, THF, EtOH, and acetone) to eliminate any extra unreacted monomers. ICP-OES measurements confirmed the existence of residual Pd in Py-*m*Azo-CMP and Py-*p*Azo-CMP, with estimated contents of 0.12 and 0.071 wt %, respectively. To determine the identities of the Py-*m*Azo and Py-*p*Azo-CMPs, FTIR and solid-state ^{13}C NMR spectroscopies were employed. The FTIR spectra of Py-*m*Azo and Py-*p*Azo-CMPs (Figure 2a)

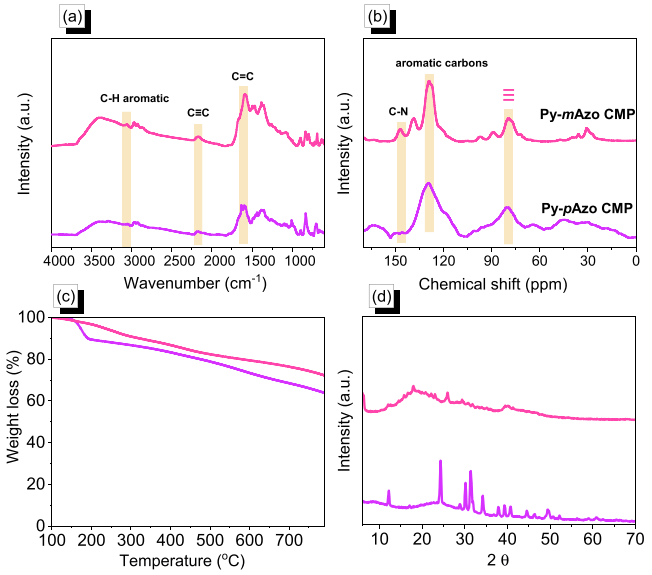

Figure 2. FTIR (a), solid-state ^{13}C NMR (b), TGA (c), and XRD (d) profiles of Py-*m*Azo and Py-*p*Azo-CMPs.

showed distinctive asymmetric and symmetric vibration peaks of the N═N functionality at 1433−1480 and 1094 cm^{-1} and 1464−1593 and 1157 cm^{-1}, respectively, to corroborate the polymer structures.[62,63] Additionally, in the ^{13}C NMR spectra, two distinct peaks at 148 ppm were observed, corresponding to carbon atoms involved in the C—N bonds of the Azo units (Figure 2b). In the range of 120−134 ppm, resonances from additional aromatic carbon atoms were found. Notably, the presence of terminal and internal alkyne carbon units in both Py-*m*Azo and Py-*p*Azo-CMPs was observed at 79.77 ppm, confirming the successful completion of the Sonogashira−Hagihara coupling between Py-T and the corresponding brominated Azo compounds. Additionally, Py-mAzo and Py-pAzo-CMPs were heated to temperatures between 40 and 800 °C for TGA (Figure 2c). At temperatures ranging from 321 to 191 °C, respectively, Py-*m*Azo and Py-*p*Azo-CMPs experienced a 10% weight loss under the N_2 atmosphere. Py-*m*Azo and Py-*p*Azo-CMPs produced char yields of 72.14% and 64% by weight, respectively, at 800 °C. These TGA results indicated that the Azo-linked CMP materials possessed enhanced thermal stability, making them promising candidates for several uses. Since all of the created Py-Azo-CMPs had some distinct crystalline peaks in their XRD profiles, it was demonstrated that all of the Py-Azo-CMPs were semicrystalline (Figure 2d).

We conducted N_2 adsorption and desorption studies at 77 K to characterize the S_{BET}, total pore volumes (V_{total}), and pore size diameters of Py-*m*Azo and Py-*p*Azo-CMPs (Figure 3). For

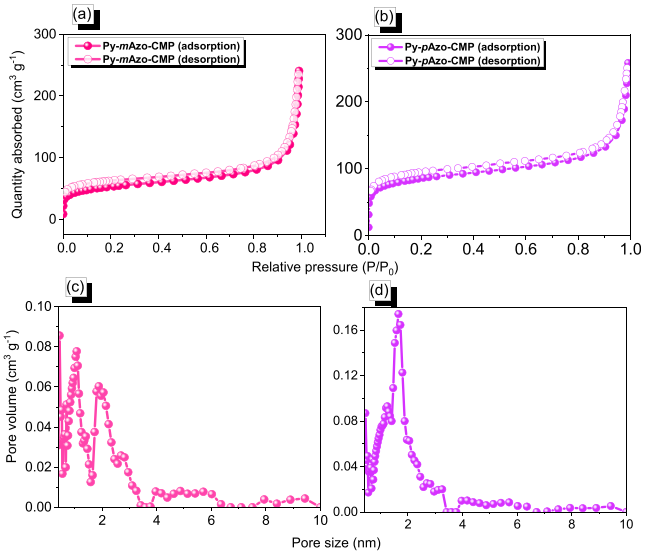

Figure 3. (a and b) BET and pore diameter distribution (c and d) profiles of Py-*m*Azo-CMP (a, c) and Py-*p*Azo-CMP (b, d).

Py-*m*Azo-CMP, we observed S_{BET} and V_{total} values of 176 m^2 g^{-1} and 0.36 cm^3 g^{-1}, respectively, while Py-*p*Azo-CMP exhibited values of 279 m^2 g^{-1} and 0.39 cm^3 g^{-1}, as depicted in Figure 3a and b. For both Py-*m*Azo and Py-*p*Azo-CMPs, we found pore diameters centered at 8.094 and 5.66 nm in their pore size distribution profiles (Figure 3c and d). Notably, the desorption processes of Py-*m*Azo and Py-*p*Azo-CMPs exhibited noticeable hysteresis, indicating the presence of mesoporous framework structures. Furthermore, the N_2 isotherm profiles of Py-*m*Azo and Py-*p*Azo-CMPs displayed type I and type IV curves in accordance with the IUPAC classification, suggesting the presence of porous structures. The disparity in the S_{BET} surface area between Py-*m*Azo and Py-*p*Azo-CMPs could be attributed to the molecular alignment of Py molecules during the polymerization process, resulting in varying degrees of polymerization. The nanoscale pore sizes observed underscored the mesoporosity of the Py-Azo-CMP frameworks.

SEM images of Py-*m*Azo-CMP and Py-*p*Azo-CMP reveal a spherical morphology with varying degrees of aggregation, as illustrated in Figure 4a−d. Furthermore, TEM images confirm the presence of porous structures within Py-Azo-CMPs, as shown in Figure 4e and f. The presence of dark spots in the TEM images was attributed to either sample aggregation or the presence of Pd nanoparticles within the Py-*m*Azo-CMP and Py-*p*Azo-CMPs. Elemental mapping of Py-*m*Azo-CMP and Py-*p*Azo-CMP, as depicted in Figure S14 through SEM-EDS analysis, revealed the presence of carbon (C) and nitrogen (N)

https://doi.org/10.1021/acsaem.3c02252
ACS Appl. Energy Mater. 2023, 6, 11342−11351

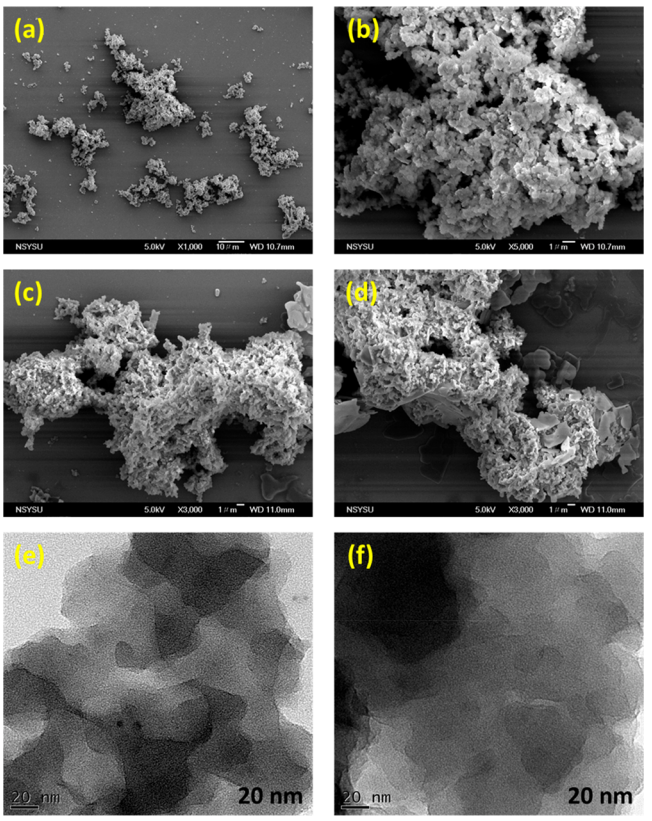

Figure 4. (a–d) SEM and (e and f) TEM images of (a, b, and e) Py-*m*Azo and (c, d, and f) Py-*p*Azo-CMPs.

elements with uniform distributions across their surfaces. In Py-*m*Azo-CMP, the atomic weights of C and N were measured at 70.02 and 29.98, respectively, while, in Py-*p*Azo-CMP, they were found to be 85.14 and 14.86, respectively.

Electrochemical Analysis of the Py-Azo-CMPs Framework. We performed an electrochemical assessment of the Py-Azo-CMPs in a KOH solution (1 M), employing galvanostatic charge–discharge (GCD) and cyclic voltammetry (CV) profiles. Figure 5a and b depict the curved CV for the complete set of Py-Azo-CMPs, encompassing a wide range of experimental conditions. We explored various scanning rates within a range of 5–200 mV s^{-1} while maintaining a potential window between −0.6 and 0.3 V. It is clear that all of the Py-Azo-CMPs displayed an unusual quasi-rectangular form in their CV profiles, regardless of the scan parameters employed. This characteristic shape indicates the presence of electric double-layer capacitance (EDLC), and the constancy of this capacitance across the different scan rates suggests a stable electrochemical performance. The CV profile of Py-*m*Azo-CMP exhibits two distinct and significant redox peaks: one oxidation peak at −0.37 V and another at −0.22 V, along with a reduction peak at −0.44 V and another at −0.28 V. These peaks, observed at 5 mV s^{-1}, are associated with the reduction in conjugation. Similarly, in the CV pattern of Py-*p*Azo-CMP, we observe two prominent redox peaks—an oxidation peak at −0.32 V and a reduction peak at −0.38 V. To further evaluate the electrochemical capabilities of Py-*m*Azo and Py-*p*Azo-CMPs, GCD measurements were performed. It was observed that the oxidation–reduction processes may not fully respond within shorter scan durations, as indicated by the CV patterns, where the capacitance decreases as the scan rate increases.

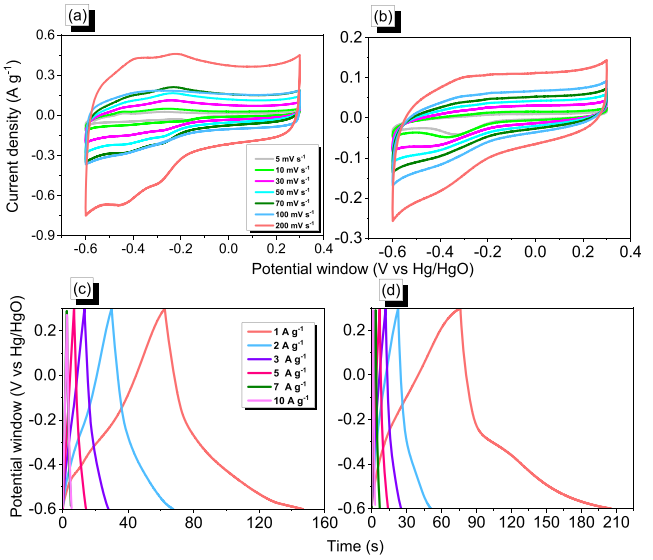

Figure 5. Py-*m*Azo-CMP (a, c), Py-*p*Azo-CMP (b, d), and their respective CV and GCD profiles were obtained in KOH (1 M).

Additionally, we examined the GCD curves and capacitance profiles over several different current densities, ranging between 1 and 20 A g^{-1} (Figure 5c and d).

These GCD curves exhibit a triangular shape with subtle bends, indicative of both electric double-layer capacitance (EDLC) and pseudocapacitance characteristics. At 1 A g^{-1}, both Py-*m*Azo and Py-*p*Azo-CMPs exhibited capacitances of 93 and 142 F g^{-1}, respectively (Figure 6a). Particularly, Py-

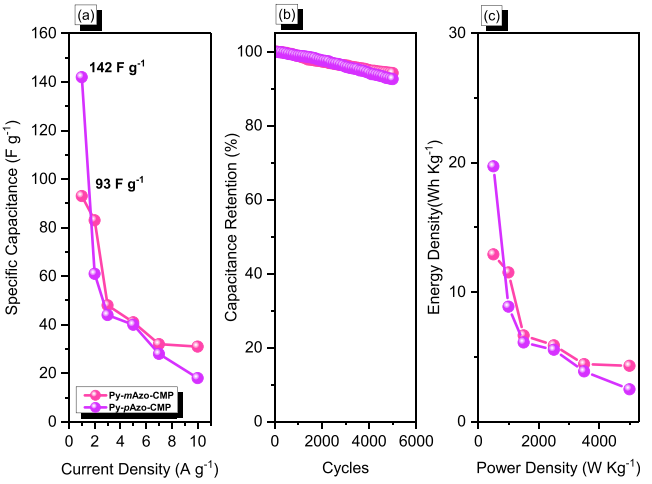

Figure 6. (a) Specific capacitance, (b) cycling stability profile, and (c) Ragone plot of Py-*m*Azo-CMP and Py-*p*Azo-CMP.

*p*Azo-CMP demonstrated superior specific capacitance compared to Py-*m*Azo-CMP, even at higher current densities. Additionally, both Py-*m*Azo and Py-*p*Azo-CMPs displayed longer discharging intervals than charging times, indicating their high capacity.[64−66] Higher capacitance resulted from the slower scan rates, which gave the ions in the electrolyte enough opportunity to interact with all of the active sites in the charged materials.[67−70] Conversely, faster scan rates facilitated more rapid access of the electrolyte to the electroactive components, leading to reduced capacitance. Additionally, Table S1 provides a comparative analysis of the specific

https://doi.org/10.1021/acsaem.3c02252
ACS Appl. Energy Mater. 2023, 6, 11342−11351

capacitance values for Py-*m*Azo and Py-*p*Azo-CMPs in comparison to previously reported materials employed in supercapacitor applications, highlighting that our materials exhibit a notably high specific capacitance. Both Py-*m*Azo and Py-*p*Azo-CMPs exhibited impressive capacity retention during 5000 cycles, with retention rates of 94.63% and 93%, respectively (Figure 6b). These results highlight the excellent cycle durability of these materials, with Py-*p*Azo-CMP demonstrating superior capacity retention compared to other porous composites. The Py-*m*Azo and Py-*p*Azo-CMP frameworks retained their spherical morphology even after undergoing 5000 cycles, as demonstrated in Figure S15. Furthermore, the Ragone plot presented in Figure 6c allowed for the determination of the energy densities of these materials. Py-*p*Azo-CMP exhibited the highest energy density at 19.72 Wh kg^{-1}, followed by Py-*m*Azo-CMP at 12.92 Wh kg^{-1}.

We investigated the interface between the electrode and the electrolyte by employing electrochemical impedance spectroscopy (EIS) over a specific frequency range. To analyze the EIS curves, we fitted them with an equivalent circuit composed of multiple components, as illustrated in Figure 7a and b. The

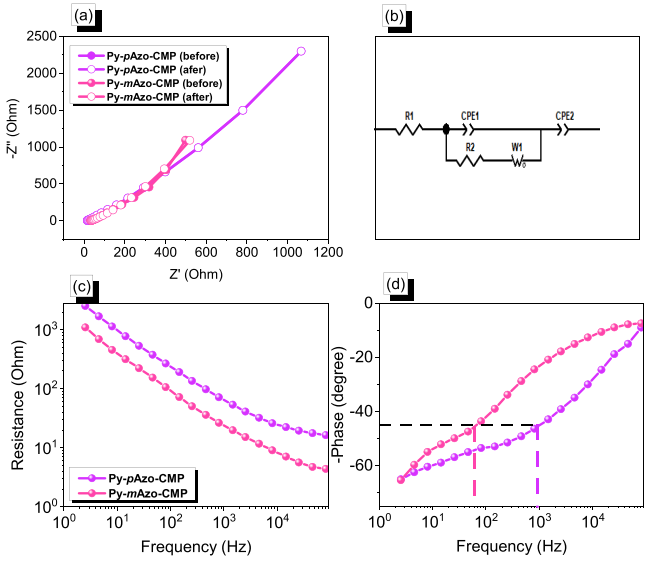

Figure 7. Electrochemical impedance spectrometry curves: (a) Nyquist plots and (b) equivalent fitted circuit, (c) Bode plot of frequency-dependent resistance (magnitude), and (d) Bode plot of frequency-dependent phase angles of Py-*m*Azo-CMP and Py-*p*Azo-CMP.

following components make up this analogous circuit: Z_w, CPE-EDLC, CPE-P, and R_s. Upon examination, Py-*m*Azo and Py-*p*Azo-CMPs exhibited initial series resistances, also known as Ohmic resistance, measuring 31.6 and 13.8 Ω, as stated. Among the two compounds, Py-*p*Azo-CMP displayed lower resistance, indicating its beneficial characteristics as an electrode material. Furthermore, the remarkable capacitive performance of these porous materials is the frequency-dependent magnitude when used as electrode materials for the energy-related application Bode plot (Figure 7c). The knee frequency, a crucial indicator of how rapidly electrode materials function, was determined from the Bode plot of the frequency-dependent phase angle (Figure 7d). The knee frequency corresponds to the point at which the capacitive and resistive characteristics of a material are balanced. Based on the information shown in Figure 7d, Py-*m*Azo and Py-*p*Azo-CMPs were discovered to have knee frequencies of 65.43 and 144.29 Hz, respectively. These outcomes show how versatile the materials are as electrode materials for energy storage systems.[67−70]

In our experiment, we utilized a CR2032 coin cell comprising multiple components (including an anode, cathode, separator, metal spring, top and bottom covers, and electrolyte). Investigating the electrochemical behavior of a symmetric supercapacitor was our main goal. In order to do this, we made use of Py-Azo-CMP materials, which were created especially for symmetric supercapacitor applications. To evaluate the symmetric supercapacitors' (SSCs) electrochemical performance, we performed CV measurements with scan rates ranging from 5 to 200 mV s^{-1} throughout a broad potential range of −0.4 to +0.4 V. Figure 8a and b show the

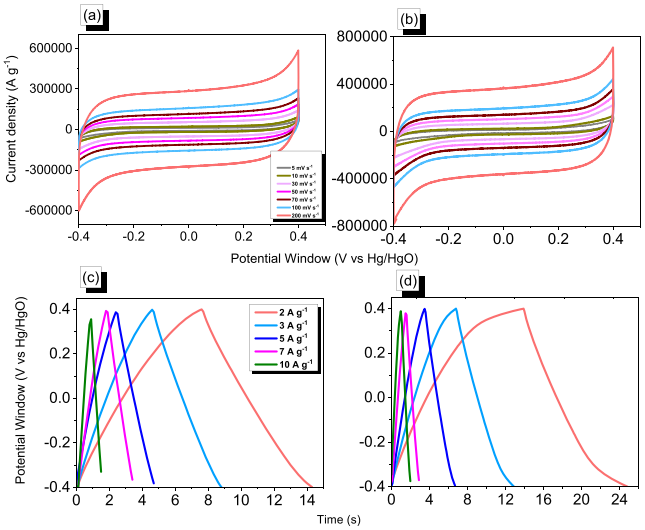

Figure 8. CV and GCD studies based on a symmetric coin cell for Py-*m*Azo-CMP (a, c) and Py-*p*Azo-CMP (b, d).

Py-Azo-CMPs' final CV curves, which had rectangular forms and peaks in the lower potential range. These characteristics are indicative of supercapacitors that possess both EDLC and pseudocapacitive behavior. Notably, as we increased the scan rate, the electrodes demonstrated excellent stability, suggesting enhanced charge−discharge capabilities and durable components. Additionally, we evaluated the performance of the Py-Azo-CMP electrodes by GCD tests, which were carried out at current densities ranging from 2 to 10 A g^{-1} (Figure 8c and d).

The GCD profiles were almost triangular forms with a few slight variations, emphasizing the advantageous interactions between EDLC and pseudocapacitance in our system. We determined that the Py-*m*Azo and Py-*p*Azo-CMPs exhibited capacitances of 17 and 28 F g^{-1}, respectively, at 2 A g^{-1} (Figure 9a). It is worth noting that the Py-*p*Azo-CMP electrode outperformed the other CMPs in terms of capacitance, likely due to its larger surface area, which enhances ion mobility within the electrode. As depicted in Figure 9b, the Py-*m*Azo and Py-*p*Azo-CMPs exhibited superior retention, with a retention rate of 98.12 and 98.32% after 5000 cycles (measured at 10 A g^{-1}). This improved stability can be due to the incorporation of heteroatoms, which enhances the connection between the electrolyte and the electrode, resulting in enhanced capacity retention. Regarding energy densities, we

https://doi.org/10.1021/acsaem.3c02252
ACS Appl. Energy Mater. 2023, 6, 11342−11351

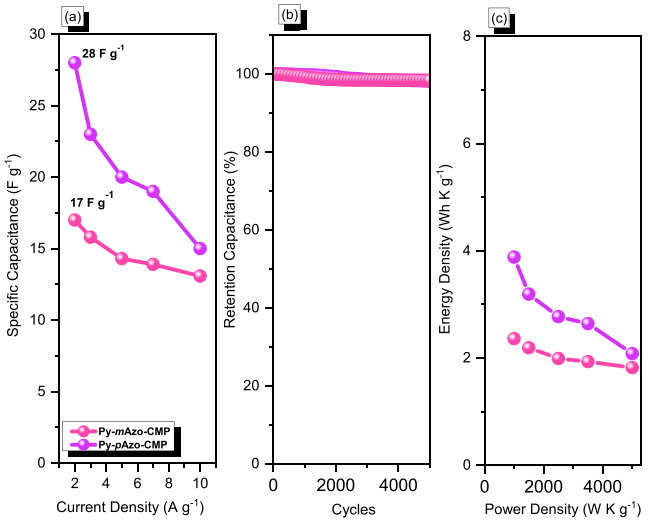

Figure 9. Capacitance (a), cycle stability (b), and Ragone plot based on a symmetric coin cell for Py-*m*Azo-CMP and Py-*p*Azo-CMP.

found that the Py-*m*Azo and Py-*p*Azo-CMPs exhibited energy densities of 2.36 and 3.88 Wh kg^{-1}, respectively, as shown in Figure 9c.

The electronic structure of Py-Azo-CMPs has a significant effect on their ability to store charge and their redox characteristics. Therefore, we conducted density functional theory (DFT) calculations using Gaussian 09W software at the B3LYP/6-31G(d) level to explore the connection between electronic structure and electrochemical performance. To account for long-range and non-covalent interactions, we incorporated the D3BJ dispersion correction. Additionally, we determined the global minimum conformer for each molecule's ground-state geometry by examining their harmonic vibrational frequencies. We used the same degree of theory to calculate the molecular electrostatic potential (MESP), lowest unoccupied molecular orbital (LUMO), and highest occupied molecular orbital (HOMO) at optimized geometries. Figure 10 depicts the Py-*m*Azo and Py-*p*Azo-CMPs' frontier molecular orbitals. For these polymers to perform electrochemically, the degree of LUMO delocalization is crucial. In both Py-*m*Azo and Py-*p*Azo-CMPs, the LUMO orbitals exhibited significant delocalization, spanning across the conjugated backbones. Furthermore, Py-*p*Azo-CMP, with its *para*-conjugation design, demonstrated improved LUMO delocalization and a narrower band gap. This design feature enhances its electrochemical performance.

Figure 11 also illustrates the MESP analyses of Py-*m*Azo and Py-*p*Azo-CMPs. The pronounced delocalization of charge density reduces the concentration of negative charges at the redox-active sites within CMPs. Faster ion diffusion and electron transfer through the CMPs' pores are made possible by this reduction's weakening of the electrolyte's contact with these active sites. In summary, these Py-*m*Azo and Py-*p*Azo-CMPs have better electrochemical performance as a consequence of their extended conjugation structures, smaller band gaps, and highly delocalized LUMO distributions.

CONCLUSION

Using the simple Sonogashira−Hagihara coupling approach, we successfully created redox-active Py-Azo-CMPs. Our work aimed to evaluate how these Py-Azo-CMPs affected the functionality of the electrode materials for supercapacitors. The synthesized Py-Azo-CMPs exhibited favorable porosity, specific regions of the surface, and char yield. According to our electrochemical assessments, Py-*p*Azo-CMP exhibited impressive capacitance values and remarkable cycle stability, enduring even after undergoing 5000 cycles. This remarkable performance can be attributed to a combination of typical EDLC and pseudocapacitance behavior. The exceptional performance of Py-*p*Azo-CMP can be attributed mainly to its heteroatom content and high specific surface area (S_{BET}). With the utilization of Py-*p*Azo-CMP, an impressive capacitance of 142 F g^{-1} was achieved. These porous Py-Azo-CMPs consistently exhibited outstanding performance when used as electrode materials in symmetric coin cells for supercapacitors, making them highly promising contenders for electrode materials. In summary, by leveraging the Sonogashira−Hagihara coupling technique, it has become possible to design and construct Azo-

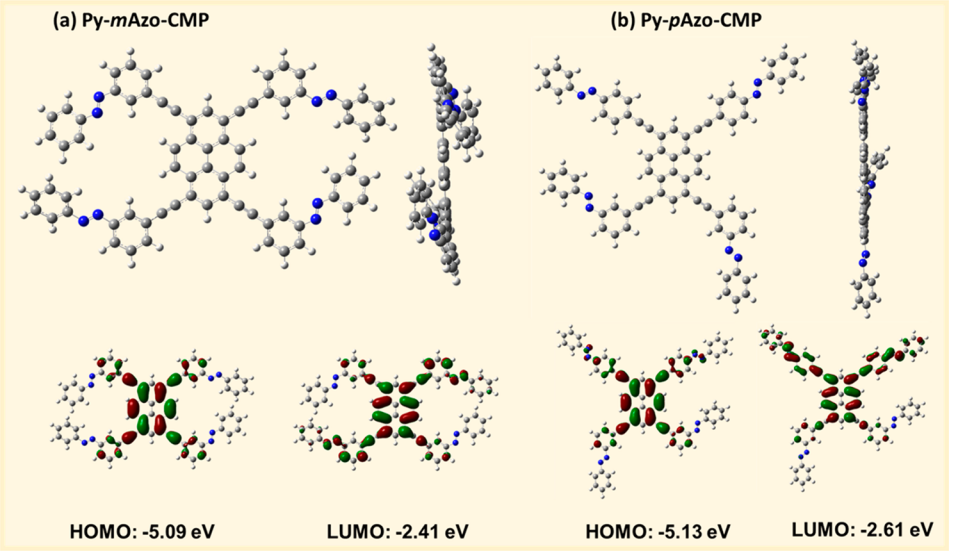

Figure 10. HOMO/LUMO and energy levels for (a) Py-*m*Azo-CMP and (b) Py-*p*Azo-CMP.

https://doi.org/10.1021/acsaem.3c02252
ACS Appl. Energy Mater. 2023, 6, 11342−11351

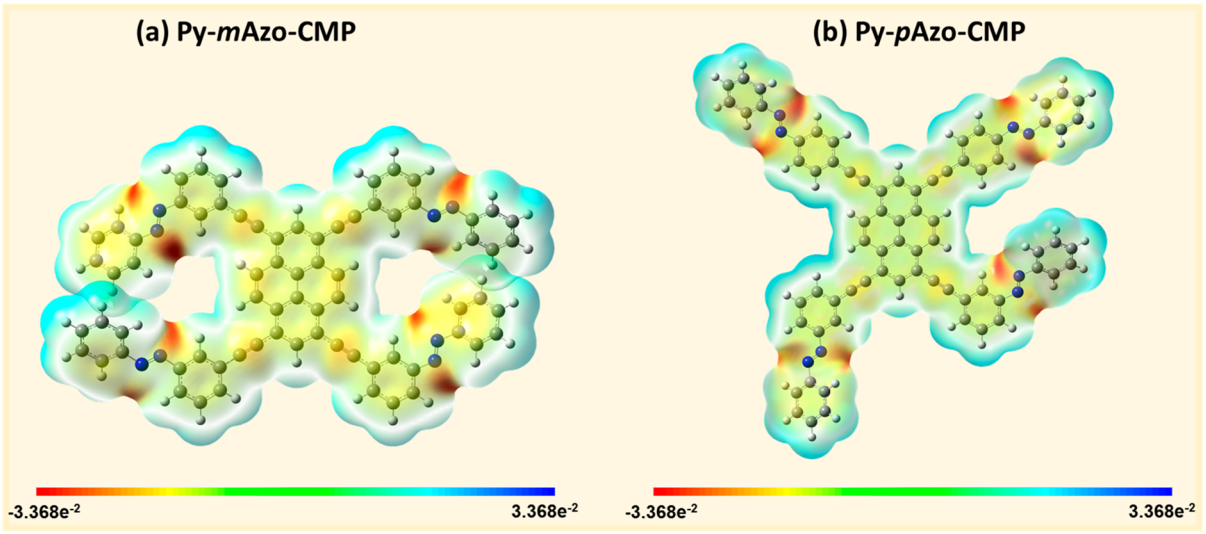

Figure 11. Electrostatic potential map on the molecular surface for (a) Py-*m*Azo-CMP and (b) Py-*p*Azo-CMP.

CMP materials featuring redox-active azo groups and exhibiting favorable physical properties.

■ ASSOCIATED CONTENT

Supporting Information

The Supporting Information is available free of charge at https://pubs.acs.org/doi/10.1021/acsaem.3c02252.

Details about the characterization methods and electrochemical analysis, DSC, FTIR, NMR, and TGA data of the synthesized *m*Azo-Br_2 and *p*Azo-Br_2, and solubility test and elemental mapping for Py-*m*Azo-CMP and Py-*p*Azo-CMP (DOCX)

■ AUTHOR INFORMATION

Corresponding Authors

Mohamed Gamal Mohamed − *Department of Materials and Optoelectronic Science, College of Semiconductor and Advanced Technology Research, Center for Functional Polymers and Supramolecular Materials, National Sun Yat-Sen University, Kaohsiung 804, Taiwan; Chemistry Department, Faculty of Science, Assiut University, Assiut 71515, Egypt;* orcid.org/0000-0003-0301-8372; Email: mgamal.eldin12@yahoo.com

Shiao-Wei Kuo − *Department of Materials and Optoelectronic Science, College of Semiconductor and Advanced Technology Research, Center for Functional Polymers and Supramolecular Materials, National Sun Yat-Sen University, Kaohsiung 804, Taiwan; Department of Medicinal and Applied Chemistry, Kaohsiung Medical University, Kaohsiung 807, Taiwan;* orcid.org/0000-0002-4306-7171; Email: kuosw@faculty.nsysu.edu.tw

Author

Poonam Nagendra Singh − *Department of Materials and Optoelectronic Science, College of Semiconductor and Advanced Technology Research, Center for Functional Polymers and Supramolecular Materials, National Sun Yat-Sen University, Kaohsiung 804, Taiwan*

Complete contact information is available at: https://pubs.acs.org/10.1021/acsaem.3c02252

Author Contributions

#P.N.S., M.G.M.: These authors contributed equally.

Notes

The authors declare no competing financial interest.

■ ACKNOWLEDGMENTS

This study was supported financially by the Ministry of Science and Technology, Taiwan, under contracts NSTC 110-2124-M-002-013 and 111-2223-E-110-004. The authors thank the staff at National Sun Yat-sen University for their assistance with the TEM (ID: EM022600) experiments.

■ REFERENCES

(1) Mohamed, M. G.; Chang, W. C.; Chaganti, S. V.; Sharma, S. U.; Lee, J. T.; Kuo, S. W. Dispersion of ultrastable crown-ether-functionalized triphenylamine and pyrene-linked porous organic conjugated polymers with single-walled carbon nanotubes as high-performance electrodes for supercapacitors. *Polym. Chem.* **2023**, *14*, 4589.

(2) Weng, T. H.; Mohamed, M. G.; Sharma, S. U.; Mekhemer, I. M. A.; Chou, H. H.; Kuo, S. W. Rationally Engineered Ultrastable Three-Dimensional (3D) Conjugated Microporous Polymers Containing Triptycene, Tetraphenylethene, and Benzothiadiazole Units as Exceptional High-Performance Organic Electrodes for Supercapacitors. *ACS Appl. Energy Mater.* **2023**, *6*, 9012−9024.

(3) Wang, F.; Wu, X.; Yuan, X.; Liu, Z.; Zhang, Y.; Fu, L.; Zhu, Y.; Zhou, Q.; Wu, Y.; Huang, W. Latest advances in supercapacitors: from new electrode materials to novel device designs. *Chem. Soc. Rev.* **2017**, *46*, 6816−6854.

(4) Singh, P. N.; Mohamed, M. G.; Chaganti, S. V.; Sharma, S. U.; Ejaz, M.; Lee, J. T.; Kuo, S. W. Rational Design of Ultrastable Conjugated Microporous Polymers based on Pyrene and Perylene Units as High-Performance Organic Electrode Materials for Supercapacitor Applications. *ACS Appl. Energy Mater.* **2023**, *6*, 8277−8287.

(5) Mohamed, M. G.; Samy, M. M.; Mansoure, T. H.; Li, C. J.; Li, W. C.; Chen, J. H.; Zhang, K.; Kuo, S. W. Microporous Carbon and Carbon/Metal Composite Materials Derived from Bio-Benzoxazine-Linked Precursor for CO_2 Capture and Energy Storage Applications. *Int. J. Mol. Sci.* **2022**, *23*, 347.

(6) Liu, S.; Kang, L.; Henzie, J.; Zhang, J.; Ha, J.; Amin, M. A.; Hossain, M. A.; Jun, S. C.; Yusuke Yamauchi, Y. Recent Advances and Perspectives of Battery-Type Anode Materials for Potassium Ion Storage. *ACS Nano* **2021**, *15*, 18931−18973.

(7) Mohamed, M. G.; Hu, H.-Y.; Madhu, M.; Samy, M. M.; Mekhemer, I. M. A.; Tseng, W.-L.; Chou, H.-H.; Kuo, S.-W. Ultrastable two-dimensional fluorescent conjugated microporous polymers containing pyrene and fluorene units for metal ion sensing and energy storage. *Eur. Polym. J.* **2023**, *189*, No. 111980.
(8) Weng, T. H.; Mohamed, M. G.; Sharma, S. U.; Chaganti, S. V.; Samy, M. M.; Lee, J. T.; Kuo, S. W. Ultrastable Three-Dimensional Triptycene- and Tetraphenylethene-Conjugated Microporous Polymers for Energy Storage. *ACS Appl. Energy Mater.* **2022**, *5*, 14239−14249.
(9) Mohamed, M. G.; Samy, M. M.; Mansoure, T. H.; Li, C. J.; Li, W. C.; Chen, J. H.; Zhang, K.; Kuo, S. W. Microporous Carbon and Carbon/Metal Composite Materials Derived from Bio-Benzoxazine-Linked Precursor for CO_2 Capture and Energy Storage Applications. *Int. J. Mol. Sci.* **2022**, *23*, 347.
(10) Ejaz, M.; Mohamed, M. G.; Kuo, S. W. Solid-state chemical transformation provides a fully benzoxazine-linked porous organic polymer displaying enhanced CO_2 capture and supercapacitor performance. *Polym. Chem.* **2023**, *14*, 2494−2509.
(11) Mohamed, M. G.; Chaganti, S. V.; Li, M. S.; Samy, M. M.; Sharma, S. U.; Lee, J. T.; Elsayed, M. H.; Chou, H. H.; Kuo, S. W. Ultrastable Porous Organic Polymers Containing Thianthrene and Pyrene Units as Organic Electrode Materials for Supercapacitors. *ACS Appl. Energy Mater.* **2022**, *5*, 6442−6452.
(12) Samy, M. M.; Mohamed, M. G.; Mansoure, T. H.; Meng, T. S.; Khan, M. A. R.; Liaw, C. C.; Kuo, S. W. Solid state chemical transformations through ring-opening polymerization of ferrocene-based conjugated microporous polymers in host−guest complexes with benzoxazine-linked cyclodextrin. *J. Taiwan Inst. Chem. Eng.* **2022**, *132*, No. 104110.
(13) Li, L.; Lu, F.; Xue, R.; Ma, B.; Li, Q.; Wu, N.; Liu, H.; Yao, W.; Guo, H.; Yang, W. Ultrastable Triazine-Based Covalent Organic Framework with an Interlayer Hydrogen Bonding for Supercapacitor Applications. *ACS Appl. Mater. Interfaces* **2019**, *11*, 26355−26363.
(14) Liu, S.; Kang, L.; Zhang, J.; Jun, S. C.; Yamauchi, Y. Sodium preintercalation-induced oxygen-deficient hydrated potassium manganese oxide for high-energy flexible Mg-ion supercapacitors. *NPG Asia Mater.* **2023**, *15*, 9.
(15) Liu, S.; Kang, L.; Jian Zhang, J.; Jung, E.; Lee, S.; Jun, S. C. Structural engineering and surface modification of MOF-derived cobalt-based hybrid nanosheets for flexible solid-state supercapacitors. *Energy Storage Mater.* **2020**, *32*, 167−177.
(16) Mohamed, M. G.; Ahmed, M. M. M.; Du, W.-T.; Kuo, S.-W. Meso/Microporous Carbons from Conjugated Hyper-Crosslinked Polymers Based on Tetraphenylethene for High-Performance CO_2 Capture and Supercapacitor. *Molecules* **2021**, *26*, 738.
(17) Liu, S.; Kang, L.; Zhang, J.; Jun, S. C.; Yamauchi, Y. Carbonaceous Anode Materials for Non-aqueous Sodium- and Potassium-Ion Hybrid Capacitors. *ACS Energy Letters* **2021**, *6*, 4127−4154.
(18) Samy, M. M.; Sharma, S. U.; Mohamed, M. G.; Mohammed, A. A. K.; Chaganti, S. V.; Lee, J. T.; Kuo, S. W. conjugated microporous polymers containing ferrocene units for high carbon dioxide uptake and energy storage. *Mater. Chem. Phys.* **2022**, *287*, No. 126177.
(19) Ejaz, M.; Samy, M. M.; Ye, Y.; Kuo, S. W.; Mohamed, M. G. Design Hybrid Porous Organic/Inorganic Polymers Containing Polyhedral Oligomeric Silsesquioxane/Pyrene/Anthracene Moieties as a High-Performance Electrode for Supercapacitor. *Int. J. Mol. Sci.* **2023**, *24*, 2501.
(20) Samy, M. M.; Mohamed, M. G.; Sharma, S. U.; Chaganti, S. V.; Lee, J. T.; Kuo, S. W. An Ultrastable Tetrabenzonaphthalene-Linked conjugated microporous polymer functioning as a high-performance electrode for supercapacitors. *J. Taiwan Inst. Chem. Eng.* **2023**, No. 104750.
(21) Mohamed, M. G.; Elsayed, M. H.; Ye, Y.; Samy, M. M.; Hassan, A. E.; Mansoure, T. H.; Wen, Z.; Chou, H.-H.; Chen, K.-H.; Kuo, S.-W. Construction of Porous Organic/Inorganic Hybrid Polymers Based on Polyhedral Oligomeric Silsesquioxane for Energy Storage and Hydrogen Production from Water. *Polymers* **2023**, *15*, 182.
(22) Mohamed, M. G.; Sharma, S. U.; Liu, N. Y.; Mansoure, T. H.; Samy, M. M.; Chaganti, S. V.; Chang, Y. L.; Lee, J. T.; Kuo, S. W. Ultrastable Covalent Triazine Organic Framework Based on Anthracene Moiety as Platform for High-Performance Carbon Dioxide Adsorption and Supercapacitors. *Int. J. Mol. Sci.* **2022**, *23*, 3174.
(23) Ye, Y. S.; Mohamed, M. G.; Chen, W. C.; Kuo, S. W. Integrating the multiple functionalities in metalloporphyrin porous organic polymers enabling strong polysulfide anchoring and rapid electrochemical kinetics in Li−S batteries. *J. Mater. Chem. A* **2023**, *11*, 9112−9124.
(24) Chen, J.; Yan, W.; Townsend, E. J.; Feng, J.; Pan, L.; Del Angel Hernandez, V.; Faul, C. F. J. Tunable Surface Area, Porosity, and Function in Conjugated Microporous Polymers. *Angew. Chem., Int. Ed.* **2019**, *58*, 11715−11719.
(25) Lee, J.-S. M.; Cooper, A. I. Advances in Conjugated Microporous Polymers. *Chem. Rev.* **2020**, *120*, 2171−2214.
(26) Mohamed, M. G.; Atayde, E. C.; Matsagar, B. M.; Na, J.; Yamauchi, Y.; Wu, K. C. W.; Kuo, S.-W. Construction Hierarchically Mesoporous/Microporous Materials Based on Block Copolymer and Covalent Organic Framework. *J. Taiwan Inst. Chem. Eng.* **2020**, *112*, 180−192.
(27) Chang, S. Y.; Elewa, A. M.; Mohamed, M. G.; Mekhemer, I. M. A.; Samy, M. M.; Zhang, K.; Chou, H. H.; Kuo, S. W. Rational design and synthesis of bifunctional Dibenzo[g,p]chrysene-based conjugated microporous polymers for energy storage and visible light-driven photocatalytic hydrogen evolution. *Mater. Today Chem.* **2023**, *33*, No. 101680.
(28) Samy, M. M.; Mekhemer, I. M. A.; Mohamed, M. G.; Elsayed, M. H.; Lin, K.-H.; Chen, Y.-K.; Wu, T.-L.; Chou, H.-H.; Kuo, S.-W. Conjugated microporous polymers incorporating Thiazolo[5,4-d]-thiazole moieties for Sunlight-Driven hydrogen production from water. *Chem, Eng. J.* **2022**, *446*, No. 137158.
(29) Das, S.; Heasman, P.; Ben, T.; Qiu, S. Porous Organic Materials: Strategic Design and Structure−Function Correlation. *Chem. Rev.* **2017**, *117*, 1515−1563.
(30) Lyu, W.; Yan, C.; Chen, Z.; Chen, J.; Zuo, H.; Teng, L.; Liu, H.; Wang, L.; Liao, Y. Spirobifluorene-Based Conjugated Microporous Polymer-Grafted Carbon Nanotubes for Efficient Supercapacitive Energy Storage. *ACS Appl. Energy Mater.* **2022**, *5*, 3706−3714.
(31) Mohamed, M. G.; Elsayed, M. H.; Elewa, A. M.; El-Mahdy, A. F. M.; Yang, C. H.; Mohammed, A. A. K.; Chou, H. H.; Kuo, S. W. Pyrene-Containing Conjugated Organic Microporous Polymers for Photocatalytic Hydrogen Evolution from Water. *Catal. Sci. Technol.* **2021**, *11*, 2229−2241.
(32) Shu, L.; Yu, J.; Cui, Y.; Ma, Y.; Li, Y.; Gao, B.; Wang, H.-G. Porphyrin-based conjugated microporous polymers with dual active sites as anode materials for lithium-organic batteries. *Int. J. Hydrogen Energy* **2022**, *47*, 10902−10910.
(33) Yuan, Y.; Zhu, G. Porous aromatic frameworks as a platform for multifunctional applications. *ACS Cent. Sci.* **2019**, *5*, 409−418.
(34) Mohamed, M. G.; EL-Mahdy, A. F. M.; Kotp, M. G.; Kuo, S. W. Advances in porous organic polymers: syntheses, structures, and diverse applications. *Mater. Adv.* **2022**, *3*, 707−733.
(35) Mohamed, M. G.; Chang, S.-Y.; Ejaz, M.; Samy, M. M.; Mousa, A. O.; Kuo, S.-W. Design and Synthesis of Bisulfone-Linked Two-Dimensional Conjugated Microporous Polymers for CO_2 Adsorption and Energy Storage. *Molecules* **2023**, *28*, 3234.
(36) Mohamed, M. G.; Mansoure, T. H.; Samy, M. M.; Takashi, Y.; Mohammed, A. A. K.; Ahamad, T.; Alshehri, S. M.; Kim, J.; Matsagar, B. M.; Wu, K. C.-W.; Kuo, S.-W. Ultrastable Conjugated Microporous Polymers Containing Benzobisthiadiazole and Pyrene Building Blocks for Energy Storage Applications. *Molecules* **2022**, *27*, 2025.
(37) Mousa, A. O.; Zheng, I. L.; Chuang, C. H.; Chen, C. K.; Kuo, S. W.; Mohamed, M. G. Rational Design of Bifunctional Microporous Organic Polymers Containing Anthracene and Triphenylamine Units for Energy Storage and Biological Applications. *Int. J. Mol. Sci.* **2023**, *24*, 8966.

https://doi.org/10.1021/acsaem.3c02252
ACS Appl. Energy Mater. 2023, 6, 11342−11351

(38) Mohamed, M. G.; Sharma, S. U.; Yang, C.-H.; Samy, M. M.; Mohammed, A. A. K.; Chaganti, S. V.; Lee, J.-T.; Kuo, S. W. Anthraquinone-Enriched Conjugated Microporous Polymers as Organic Cathode Materials for High-Performance Lithium-Ion Batteries. *ACS Appl. Energy Mater.* **2021**, *4*, 14628−14639.
(39) Zhang, B.; Wang, W.; Liang, L.; Xu, Z.; Li, X.; Qiao, S. Prevailing conjugated porous polymers for electrochemical energy storage and conversion: Lithium-ion batteries, supercapacitors and water-splitting. *Coord. Chem. Rev.* **2021**, *436*, No. 213782.
(40) Snell, K. E.; Mevellec, J.-Y.; Humbert, B.; Lagugné-Labarthet, F.; Ishow, E. Photochromic Organic Nanoparticles as Innovative Platforms for Plasmonic Nanoassemblies. *ACS Appl. Mater. Interfaces* **2015**, *7*, 1932−1942.
(41) Shimizu, T.; Tanifuji, N.; Yoshikawa, H. A.-O. Azo Compounds as Active Materials of Energy Storage Systems. *Angew. Chem., Int. Ed.* **2022**, *61*, No. e202206093.
(42) Goujon, N.; Casado, N.; Patil, N.; Marcilla, R.; Mecerreyes, D. Organic batteries based on just redox polymers. *Prog. Polym. Sci.* **2021**, *122*, No. 101449.
(43) Ma, W.; Luo, L.-W.; Dong, P.; Zheng, P.; Huang, X.; Zhang, C.; Jiang, J.-X.; Cao, Y. Toward High-Performance Dihydrophenazine-Based Conjugated Microporous Polymer Cathodes for Dual-Ion Batteries through Donor−Acceptor Structural Design. *Adv. Funct. Mater.* **2021**, *31*, No. 2105027.
(44) Zhang, S.; Xing, F.; Chen, L.; Wang, X.; He, X. Tuning the Azo Location in Conjugated Polymers Toward High-Performance Lithium-Ion Batteries. *Chem. Mater.* **2022**, *34* (20), 9031−9041.
(45) Cheng, Y.-J.; Yang, S.-H.; Hsu, C.-S. Synthesis of Conjugated Polymers for Organic Solar Cell Applications. *Chem. Rev.* **2009**, *109*, 5868−5923.
(46) Dou, L.; Liu, Y.; Hong, Z.; Li, G.; Yang, Y. Low-Bandgap Near-IR Conjugated Polymers/Molecules for Organic Electronics. *Chem. Rev.* **2015**, *115*, 12633−12665.
(47) Guan, X.; Zhao, Y.; Pei, H.; Zhao, M.; Wang, Y.; Zhou, X.; Mohamed, M. G.; Kuo, S. W.; Ye, Y. Metalloporphyrin conjugated porous polymer in-situ grown on a Celgard separator as multifunctional polysulfide barrier and catalyst for high-performance Li-S batteries. *Chem. Eng. J.* **2023**, *473*, No. 144733.
(48) Xu, Y.; Mao, N.; Zhang, C.; Wang, X.; Zeng, J.; Chen, Y.; Wang, F.; Jiang, J.-X. Rational design of donor-π-acceptor conjugated microporous polymers for photocatalytic hydrogen production. *Appl. Catal., B* **2018**, *228*, 1−9.
(49) Kwon, J.; Hong, J.-P.; Noh, S.; Kim, T.-M.; Kim, J.-J.; Lee, C.; Lee, S.; Hong, J.-I. Pyrene end-capped oligothiophene derivatives for organic thin-film transistors and organic solar cells. *New J. Chem.* **2012**, *36*, 1813−1818.
(50) Tao, J.; Liu, D.; Qin, Z.; Shao, B.; Jing, J.; Li, H.; Dong, H.; Xu, B.; Tian, W. Organic UV-Sensitive Phototransistors Based on Distriphenylamineethynylpyrene Derivatives with Ultra-High Detectivity Approaching 1018. *Adv. Mater.* **2020**, *32*, No. 1907791.
(51) Mohamed, M. G.; Chaganti, S. V.; Sharma, S. U.; Samy, M. M.; Ejaz, M.; Lee, J.-T.; Zhang, K.; Kuo, S.-W. Constructing Conjugated Microporous Polymers Containing the Pyrene-4,5,9,10-Tetraone Unit for Energy Storage. *ACS Appl. Energy Mater.* **2022**, *5*, 10130−10140.
(52) Samy, M. M.; Mohamed, M. G.; Kuo, S.-W. Pyrene-functionalized tetraphenylethylene polybenzoxazine for dispersing single-walled carbon nanotubes and energy storage. *Compos. Sci. Technol.* **2020**, *199*, No. 108360.
(53) Mohamed, M. G.; Samy, M. M.; Mansoure, T. H.; Sharma, S. U.; Tsai, M.-S.; Chen, J.-H.; Lee, J.-T.; Kuo, S.-W. Dispersions of 1,3,4-Oxadiazole-Linked Conjugated Microporous Polymers with Carbon Nanotubes as a High-Performance Electrode for Supercapacitors. *ACS Appl. Energy Mater.* **2022**, *5*, 3677−3688.
(54) Kinik, F. P.; Ortega-Guerrero, A.; Ongari, D.; Ireland, C. P.; Smit, B. Pyrene-based metal organic frameworks: From synthesis to applications. *Chem. Soc. Rev.* **2021**, *50*, 3143−3177.
(55) Qin, J.-H.; Zhang, J.-R.; Xiao, Z.; Wu, Y.-P.; Xu, H.-M.; Yang, X.-G.; Ma, L.-F.; Li, D.-S. Topology- and guest-dependent photoelectric conversion of 2d anionic pyrene-based metal−organic framework. *Cryst. Growth Des.* **2022**, *22*, 4018−4024.
(56) Qin, J.-H.; Huang, Y.-D.; Zhao, Y.; Yang, X.-G.; Li, F.-F.; Wang, C.; Ma, L.-F. Highly dense packing of chromophoric linkers achievable in a pyrene-based metal-organic framework for photoelectric response. *Inorg. Chem.* **2019**, *58*, 15013−15016.
(57) Mousa, A. O.; Mohamed, M. G.; Chuang, C.-H.; Kuo, S.-W. Carbonized Aminal-Linked Porous Organic Polymers Containing Pyrene and Triazine Units for Gas Uptake and Energy Storage. *Polymers* **2023**, *15*, 1891.
(58) Mohamed, M. G.; Samy, M. M.; Mansoure, T. H.; Li, C.-J.; Li, W.-C.; Chen, J.-H.; Zhang, K.; Kuo, S.-W. Microporous Carbon and Carbon/Metal Composite Materials Derived from Bio-Benzoxazine-Linked Precursor for CO_2 Capture and Energy Storage Applications. *Int. J. Mol. Sci.* **2022**, *23*, 347.
(59) Mousa, A. O.; Mohamed, M. G.; Lin, Z. I.; Chuang, C. H.; Chen, C. K.; Kuo, S. W. Conjugated microporous polymers as a novel generation of drug carriers: A systemic study toward efficient carriers of tetracycline antibiotic. *Eur. Polym. J.* **2023**, *196*, No. 112254.
(60) Mohamed, M. G.; Chang, W. C.; Kuo, S. W. Crown Ether- and Benzoxazine-Linked Porous Organic Polymers Displaying Enhanced Metal Ion and CO_2 Capture through Solid-State Chemical Transformation. *Macromolecules* **2022**, *55*, 7879−7892.
(61) Mohamed, M. G.; Chen, T. C.; Kuo, S. W. Solid-State Chemical Transformations to Enhance Gas Capture in Benzoxazine-Linked Conjugated Microporous Polymers. *Macromolecules* **2021**, *54*, 5866−5877.
(62) Zhu, Y.; Zhang, W. Reversible tuning of pore size and CO_2 adsorption in azobenzene functionalized porous organic polymers. *Chem. Sci.* **2014**, *5*, 4957−4961.
(63) Yang, Z.; Yu, B.; Zhang, H.; Zhao, Y.; Chen, Y.; Ma, Z.; Ji, G.; Gao, X.; Han, B.; Liu, Z. Metalated mesoporous poly (triphenylphosphine) with azo functionality: efficient catalysts for CO_2 conversion. *ACS Catal.* **2016**, *6*, 1268−1273.
(64) Ma, Y.; Lu, N.; Hu, Z.; Zhang, J.; Cao, X.; Li, J.; Zhu, Z.; Sun, H.; Liang, W.; Li, A. Carbonized conjugated microporous polymers hollow spheres incorporated with fatty alcohols for ultra-highly efficient energy storage and conversion. *Sol. Energy Mater. Sol.* **2023**, *250*, No. 112076.
(65) Dai, Y.; Wang, Y.; Xu, H.; Li, X.; Yan, X.; Xu, X. Structure, morphology and energy storage properties of imide conjugated microporous polymers with different cores and the corresponding composites with CNT. *Electrochim. Acta* **2023**, *441*, No. 141820.
(66) Chen, W.-C.; Wen, T.-C.; Teng, H. Polyaniline-deposited porous carbon electrode for supercapacitor. *Electrochim. Acta* **2003**, *48*, 641−649.
(67) Rafik, F.; Gualous, H.; Gallay, R.; Crausaz, A.; Berthon, A. Frequency, thermal and voltage supercapacitor characterization and modeling. *J. Power Sources* **2007**, *165*, 928−934.
(68) Zheng, L.; Tang, B.; Dai, X.; Xing, T.; Ouyang, Y.; Wang, Y.; Chang, B.; Shu, H.; Wang, X. High-yield synthesis of N-rich polymer-derived porous carbon with nanorod-like structure and ultrahigh N-doped content for high-performance supercapacitors. *Chem. Eng. J.* **2020**, *399*, No. 125671.
(69) Samy, M. M.; Mohamed, M. G.; Kuo, S. W. Conjugated Microporous Polymers Based on Ferrocene Units as Highly Efficient Electrodes for Energy Storage. *Polymers* **2023**, *15*, 1095.
(70) Samy, M. M.; Mohamed, M. G.; Sharma, S. U.; Chaganti, S. V.; Mansoure, T. H.; Lee, J. T.; Chen, T.; Kuo, S. W. Constructing conjugated microporous polymers containing triphenylamine moieties for high-performance capacitive energy storage. *Polymer* **2023**, *264*, No. 125541.

https://doi.org/10.1021/acsaem.3c02252
ACS Appl. Energy Mater. 2023, 6, 11342−11351